Biogeosciences, 20, 405–420, 2023
https://doi.org/10.5194/bg-20-405-2023

Biogeosciences Open Access EGU

Tracing differences in iron supply to the Mid-Atlantic Ridge valley between hydrothermal vent sites: implications for the addition of iron to the deep ocean

Alastair J. M. Lough[1,a], Alessandro Tagliabue[2], Clément Demasy[1], Joseph A. Resing[3], Travis Mellett[4], Neil J. Wyatt[1], and Maeve C. Lohan[1]

[1]Ocean & Earth Science, University of Southampton, Southampton SO14 3ZH, UK
[2]Earth, Ocean & Ecological Sciences, Liverpool L69 3BX, UK
[3]Cooperative Institute for Climate, Oceans, and Ecosystem Studies,
University of Washington and NOAA-PMEL, Seattle, WA 98115, USA
[4]College of Marine Science, University of South Florida, St. Petersburg, FL 33701, USA
[a]now at: School of Geography, University of Leeds, Leeds, LS2 9JT, UK

Correspondence: Alastair J. M. Lough (a.j.m.lough@leeds.ac.uk)

Received: 18 March 2022 – Discussion started: 4 April 2022
Revised: 18 October 2022 – Accepted: 8 November 2022 – Published: 25 January 2023

Abstract. Supply of iron (Fe) to the surface ocean supports primary productivity, and while hydrothermal input of Fe to the deep ocean is known to be extensive it remains poorly constrained. Global estimates of hydrothermal Fe supply rely on using dissolved Fe (dFe) to excess He (xs^3He) ratios to upscale fluxes, but observational constraints on dFe/xs^3He may be sensitive to assumptions linked to sampling and interpolation. We examined the variability in dFe/xs^3He using two methods of estimation, for four vent sites with different geochemistry along the Mid-Atlantic Ridge. At both Rainbow and TAG, the plume was sampled repeatedly and the range of dFe/xs^3He was 4 to 63 and 4 to 87 nmol:fmol, respectively, primarily due to differences in plume age. To account for background xs^3He and shifting plume position, we calibrated He values using contemporaneous dissolved Mn (dMn). Applying this approach more widely, we found dFe/xs^3He ratios of 12, 4–8, 4–44, and 4–86 nmol fmol^{-1} for the Menez Gwen, Lucky Strike, Rainbow, and TAG hydrothermal vent sites, respectively. Differences in plume dFe/xs^3He across sites were not simply related to the vent endmember Fe and He fluxes. Within 40 km of the vents, the dFe/xs^3He ratios decreased to 3–38 nmol fmol^{-1}, due to the precipitation and subsequent settling of particulates. The ratio of colloidal Fe to dFe was consistently higher (0.67–0.97) than the deep N. Atlantic (0.5) throughout both the TAG and Rainbow plumes, indicative of Fe exchange between dissolved and particulate phases. Our comparison of TAG and Rainbow shows there is a limit to the amount of hydrothermal Fe released from vents that can form colloids in the rising plume. Higher particle loading will enhance the longevity of the Rainbow hydrothermal plume within the deep ocean assuming particles undergo continual dissolution/disaggregation. Future studies examining the length of plume pathways required to escape the ridge valley will be important in determining Fe supply from slow spreading mid-ocean ridges to the deep ocean, along with the frequency of ultramafic sites such as Rainbow. Resolving the ridge valley bathymetry and accounting for variability in vent sources in global biogeochemical models will be key to further constraining the hydrothermal Fe flux.

1 Introduction

Iron (Fe) is an essential trace element that shapes ocean biogeochemical cycles. Photosynthetic primary productivity and nitrogen fixation in the surface ocean depend on the supply of Fe from lithogenic sources. Predicting the extent to which primary productivity is limited by Fe supply is dependent on our understanding of Fe sources and sinks in the open ocean

(Tagliabue et al., 2017). This is particularly important in Fe-limited regions such as the Southern Ocean, where changes in the supply of Fe to the surface ocean may dramatically shift the Earth's atmospheric CO_2 content (Gottschalk et al., 2019) and where hydrothermal vents may play an important role as a source of Fe (Tagliabue et al., 2010; Tagliabue and Resing, 2016; Ardyna et al., 2019; Weber, 2020; Schine et al., 2021).

The magnitude and importance of Fe supplied from different sources (i.e. glaciers, rivers, aerosols, sediments and hydrothermal vents) is an ongoing subject of debate. In the last 15 years, the role of hydrothermal vents in supplying Fe to the deep ocean, that may subsequently upwell in the Southern Ocean, has received significant attention, with questions surrounding the biogeochemical processes that could facilitate long-range transport of Fe from the seafloor (Toner et al., 2009; Tagliabue et al., 2010; Yucel et al., 2011; Saito et al., 2013; Resing et al., 2015; Fitzsimmons et al., 2017). In order to examine the hydrothermal flux of Fe to the deep ocean, changes in Fe concentration are frequently compared to excess helium (xs^3He), derived from δ^3He, which is an inert tracer of hydrothermal activity (Lupton and Craig, 1981; Wu et al., 2011; Saito et al., 2013; Resing et al., 2015; Fitzsimmons et al., 2017). Primordial helium (He) degasses from the Earth's mantle and as a result hydrothermal fluids are enriched in ^3He relative to background seawater (Lupton et al., 1977). As He is an unreactive dissolved gas, it is an ideal source tracer for hydrothermal plumes. The ratio of Fe to xs^3He has been used as a basis for modelling the impact of hydrothermal Fe on surface ocean primary productivity and the associated carbon export (Tagliabue et al., 2010).

Recent field studies have found a linear relationship between dissolved Fe (dFe) and xs^3He, interpreted as conservative behaviour of Fe. In some cases, Fe appears to behave conservatively over thousands of kilometres, while in others the conservative relationship of dFe/xs^3He is only apparent over the ridge (Saito et al., 2013; Resing et al., 2015). The observation of conservative behaviour was unexpected for a reactive metal such as Fe, as previous studies working at the < 1 km scale had estimated that up to $\sim 90\,\%$ of Fe released from seafloor vents precipitates as Fe-sulfide and Fe-oxyhydroxide mineral particles, as the Fe and hydrogen sulfide (H_2S) rich vent fluids are released into cold, well-oxygenated, deep ocean waters (German et al., 1991; Field and Sherrell, 2000; Severmann et al., 2004). It is the remaining hydrothermal Fe that does not form fast settling mineral particles that is ultimately exported, as an effective flux to the deep ocean of fine colloidal particles and/or organic Fe complexes (Bennett et al., 2008; Hawkes et al., 2013; Kleint et al., 2016). It is thought that the off-axis linear relationship of dFe with xs^3He arises because dFe species formed in the plume exhibit relatively unreactive behaviour (Bennett et al., 2008; Yucel et al., 2011). An alternative hypothesis is that Fe is added to the dissolved fraction continuously by the dissolution/disaggregation of larger particulate phases as the plume disperses (Fitzsimmons et al., 2017), at a rate that maintains the dFe/xs^3He ratio, giving the appearance of conservative behaviour.

Studies that have used xs^3He as a tool for understanding hydrothermal Fe have typically sampled at the basin scale whereas studies focusing on the < 1 km scale tend to use other shorter lived tracers such as dissolved manganese (dMn) (James and Elderfield, 1996; Field and Sherrell, 2000; Lough et al., 2017, 2019b, a), magnesium (Findlay et al., 2015) or rare earth element anomalies (Severmann et al., 2004). Furthermore, the Fe and He sampled at the basin scale may represent an amalgamation of several vent sources from a ridge or several ridge crests whereas the studies at < 1 km scale focus on Fe released from individual or at least fewer vent sites. Different vent sites are known to display substantial variations in dFe/xs^3He ratios (Table 1) (Tagliabue et al., 2010) but the extent to which sampling scale, strategy and use of different tracers affects the interpretation of the effective hydrothermal iron flux is a barrier to further refining the conceptual and numerical models we rely on for larger scale integration.

To address this knowledge gap, this study sampled hydrothermal plumes along the same ridge from multiple vent sources at a scale of 10's of km's, using both short-lived (dMn, weeks; Cowen et al., 1990; Trocine and Trefry, 1988; Field and Sherrell, 2000; Massoth et al., 1994; Lavelle et al., 1992) and long-lived (xs^3He) as conservative tracers. We examined the variability in dFe/xs^3He produced from different methods of estimation (Saito et al., 2013; Resing et al., 2015; Fitzsimmons et al., 2017) in plumes originating from four vent sites along the northern part of the Mid-Atlantic Ridge (MAR) (GEOTRACES GA13 section). These vents cover a range of geological settings, plume dFe concentrations and importantly Fe/H_2S ratios, which have been shown to correlate with colloid concentration in nascent plumes (i.e. 1–2 m above the vents) (Gartman et al., 2014). Calculated Fe/xs^3He values are used to compare the separation of Fe between particulate-dissolved fractions for the TAG and Rainbow plumes as they disperse within the ridge valley.

2 Methods

2.1 Sample collection

The UK GEOTRACES GA13 voyage sailed along the northern Mid-Atlantic Ridge (MAR) during its passage from Southampton, UK, to Guadeloupe, France (22 December 2017–27 January 2018). The fieldwork campaign sampled the rising buoyant and neutrally-buoyant hydrothermal plumes of a set of known hydrothermal vent sites along the northern MAR (Fig. 1). At each site, hydrothermal plumes were detected using a combination of sensors. A traditional CTD (conductivity–temperature–depth) package (Seabird 911) was used to identify anomalous changes in

Table 1. Summary of average endmember vent fluid data taken from the InteRidge database (Beaulieu et al., 2013).

Vent field	Geology	T (°C)	Cl^- (mM)	pH	^3He fmol kg^{-1}	Fe nmol kg^{-1}	Mn nmol kg^{-1}	H_2S (mM)	dFe/xs^{3}He (nmol fmol^{-1})	dFe/H_2S (mmol mmol^{-1})
Menez Gwen	E-MORB	285	335	4.4	2.0×10^4	1.4×10^4	7.1×10^4	1.53	1	0.01
Lucky Strike	E-MORB	301	493	3.5	1.0×10^4	5.61×10^5	2.62×10^5	3.08	47	0.18
Rainbow	Serpentinite, gabbro, MORB	366	750	2.9	2.5×10^4	2.41×10^7	1.96×10^6	0.93	962	25.86
TAG	MORB	359	661	3.2	1.8×10^4	5.11×10^6	5.52×10^5	5.13	249	1.00

MORB is mid-ocean ridge basalt; E-MORB is enriched mid-ocean ridge basalt. Endmember vent fluid data from published studies are calculated by extrapolating to 0 Mg concentration (Douville et al., 2002).

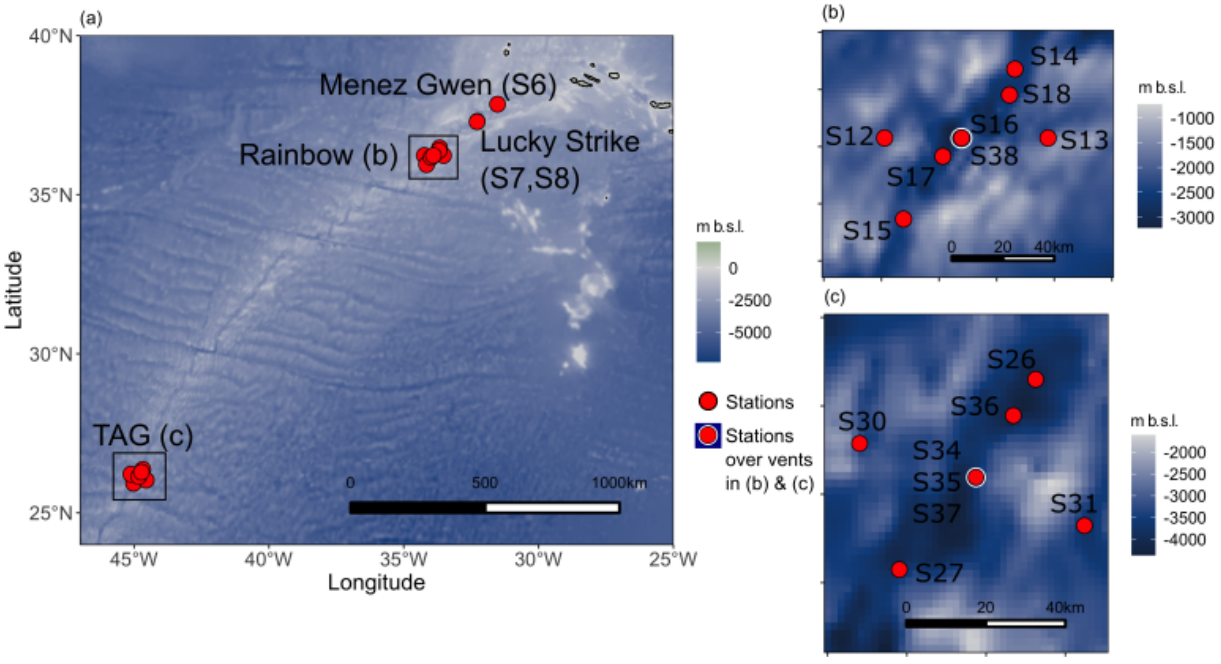

Figure 1. **(a)** Map showing the location of the main vent sites sampled during the GA13 voyage and the nearby stations within 40 km of each site at Rainbow **(b)** and TAG **(c)**. Bathymetry data are sourced from the National Oceanic and Atmospheric Administration (NOAA) ETOP1. Maps were produced in R studio using the marmap package.

salinity and temperature relative to background N. Atlantic waters. Bespoke light scattering (LSS) and oxidation reduction potential (ORP) sensors were used to identify particle dense plumes and young plume waters containing reducing chemical species (i.e. Fe^{2+}, HS^- and H_2). Sampling casts were repeated over the TAG and Rainbow sites to examine the reproducibility of plume sampling relative to tidal forces and bottom currents that shift the plumes position in the water column.

As part of the GEOTRACES programme, Fe and Mn were sampled according to the detailed procedures described previously (Cutter et al., 2010) that we briefly outline below. However, He and additional Mn samples were collected from a standard (stainless steel) rosette, and we show that Mn can be sampled cleanly without a clean lab or a titanium rosette frame (Fig. S1 in the Supplement).

Helium sampling methods followed those described in Jenkins et al. (2015b). Briefly, 30 in. of copper pipe was rinsed several times through with seawater collected from Niskin bottles (Ocean Test Equipment) on the standard rosette, using plastic tubing (TYGON). Once all air bubbles had been removed, the copper tubing was crimped at both ends to seal the pipe and sent for analysis at Woods Hole Oceanographic Institution (USA).

$$\delta^3\mathrm{He} = \left(\frac{(^3\mathrm{He}/^4\mathrm{He})_x}{(^3\mathrm{He}/^4\mathrm{He})_{\mathrm{Air}}} - 1 \right) \times 100\,\% \quad (1)$$

$$\mathrm{xs}^3\mathrm{He} = (\delta^3\mathrm{He} - -1.7) \div 100 \times [\mathrm{He}] \times 1.384 \times 10^{-6} \quad (2)$$

The δ^3He isotope anomaly is defined relative to an atmospheric standard in Eq. (1) with δ^3He expressed in percent. The xs^{3}He represents the mantle derived ^{3}He that is approxi-

mate to the non-atmospheric ^{3}He over saturation. The He isotope ratio anomaly 1.384×10^{-6} is the atmospheric ^{3}He/^{4}He ratio, [He] is the molar concentration of He and -1.7 is the solubility equilibrium constant (Jenkins et al., 2015a).

Seawater samples for trace metal analysis were collected using a titanium-frame CTD with 24 trace metal clean, 10 L, Teflon-coated Niskin bottles (Ocean Test Equipment) deployed on a plasma rope. A Sartobran 300 (Sartorius) filter capsule (0.2 µm) was used to filter seawater into clean low-density polyethylene (LDPE) bottles for dissolved trace metals. A separate aliquot of 0.2 µm filtered seawater was further filtered through 0.02 µm syringe filters (Anotop, Whatman) into LDPE bottles for soluble Fe (sFe) (Ussher et al., 2010). Unfiltered seawater samples were collected for total dissolvable (TD) metals. All samples were acidified onboard to 0.024 M (UpA HCl, ROMIL).

2.2 Sample analysis

Dissolved and total dissolvable samples were analysed onshore for Fe and Mn by ICP-MS (Thermo Scientific, Element XR) using a standard addition method (Lough et al., 2017). Certified values for GEOTRACES reference material D2 (0.96 nM Fe and 0.36 nM Mn) compared well with our measured values of 0.95 ± 0.06 nM Fe and 0.34 ± 0.03 nM Mn ($n = 6$). ICP-MS analysis of 2009 GEOTRACES coastal surface seawater (GSC) reference material (measured GSC: 2.04 ± 0.03 nM Mn and 1.48 ± 0.13 nM Fe $n = 3$) also compared well with the preliminary consensus values (GSC 2.18 ± 0.08 nM Mn, 1.54 ± 0.12 nM Fe). In-house standards with higher concentrations of Fe and Mn in the concentration range of hydrothermal samples were measured repeatedly with relative standard deviations of 6 % for Mn and 7 % for Fe. Soluble Fe was measured by flow injection analysis with chemiluminescence detection (Obata et al., 1993; Kunde et al., 2019a) with measured values of 0.94 ± 0.04 ($n = 6$) for D2 reference material. Measurements of 2009 GEOTRACES Pacific surface seawater (GSP) and GSC reference materials using flow injection also agree with the preliminary consensus values (consensus: GSP 0.16 ± 0.05, GSC 1.54 ± 0.12 nM, measured GSP 0.15 ± 0.01 nM $n = 7$, GSC 1.52 ± 0.06, $n = 10$). Colloidal Fe (cFe) is operationally defined as the difference between dFe (< 0.2 µm) and sFe (< 0.02 µm). Apparent particulate Fe (appPFe) is further operationally defined as the difference between TDFe (unfiltered) and dFe (< 0.2 µm).

Dissolved Mn samples from the standard rosette were analysed at sea by flow injection analysis with in-line pre-concentration on resin-immobilised 8-hydroxyquinoline and colorimetric detection (Resing and Mottl, 1992). The SAFe reference samples were analysed to determine the accuracy and precision of the method giving results for SAFe S, 0.82 ± 0.06 nM ($n = 19$; consensus value $= 0.79 \pm 0.06$ nM); for SAFe D2, 0.41 ± 0.03 nM ($n = 18$; consensus value $= 0.35 \pm 0.05$).

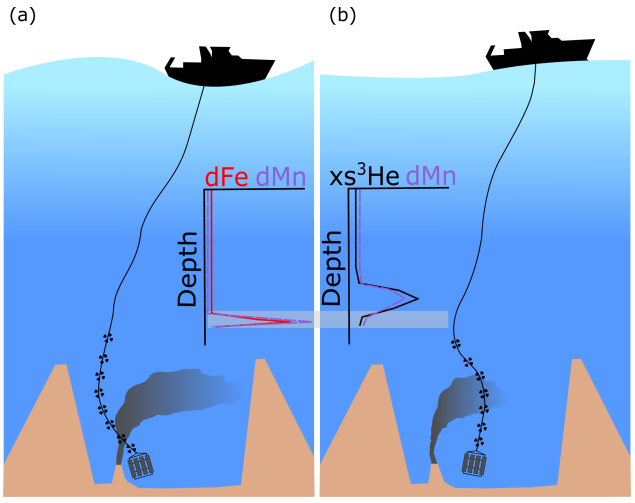

Figure 2. Schematic diagram illustrating the difficulties in sampling different elements at the same stage of a plume over a vent site using separate trace metal clean **(a)** and standard casts **(b)**. The targets on the black lines represent depths sampled in the water column. The grey shaded area indicates where there are samples taken at the same depth for xs^{3}He and dFe. Notice that at the same depth for different casts dFe is increasing with depth whilst xs^{3}He is decreasing with depth due to the offset in the plume anomaly.

Samples collected for helium analysis were quantitatively gas-extracted from Cu sampling pipes into 30 mL glass vials and analysed for helium isotope ratios. Analysis was conducted using a triple quadrupole mass filter mass spectrometer (HIDEN P/N PCI 1000 1.2HAL/3F 1301-9 PIC type 570,309). Measurements have a precision of 0.1 % as determined by repeat measurements of gas standards, all measurements of gas abundances are references to a marine atmospheric standard. Full details of helium gas analysis are described in (Jenkins et al., 2019).

3 Results and discussion

3.1 Quantifying Fe/xs^{3}He ratios

A drawback to using xs^{3}He as a tracer of hydrothermal Fe is that Fe, under GEOTRACES protocols, is sampled using trace metal clean bottles mounted on a trace metal clean rosette, while He is sampled separately from a standard rosette to avoid metal contamination from Cu tubes used to collect ^{3}He. At the Fe concentrations observed close to the vent sites, such caution is likely unwarranted; however, to trace the full reach of a hydrothermal plume, trace concentrations 0.1 nM above background concentrations need to be detected. The best way to guarantee this resolution is to follow GEOTRACES trace metal clean sampling protocols; as a result, Fe and ^{3}He are never sampled from the same sampling bottle, same cast or at the same time (Fig. 2). Furthermore, sampling ^{3}He requires the Cu pipes to be flushed with co-

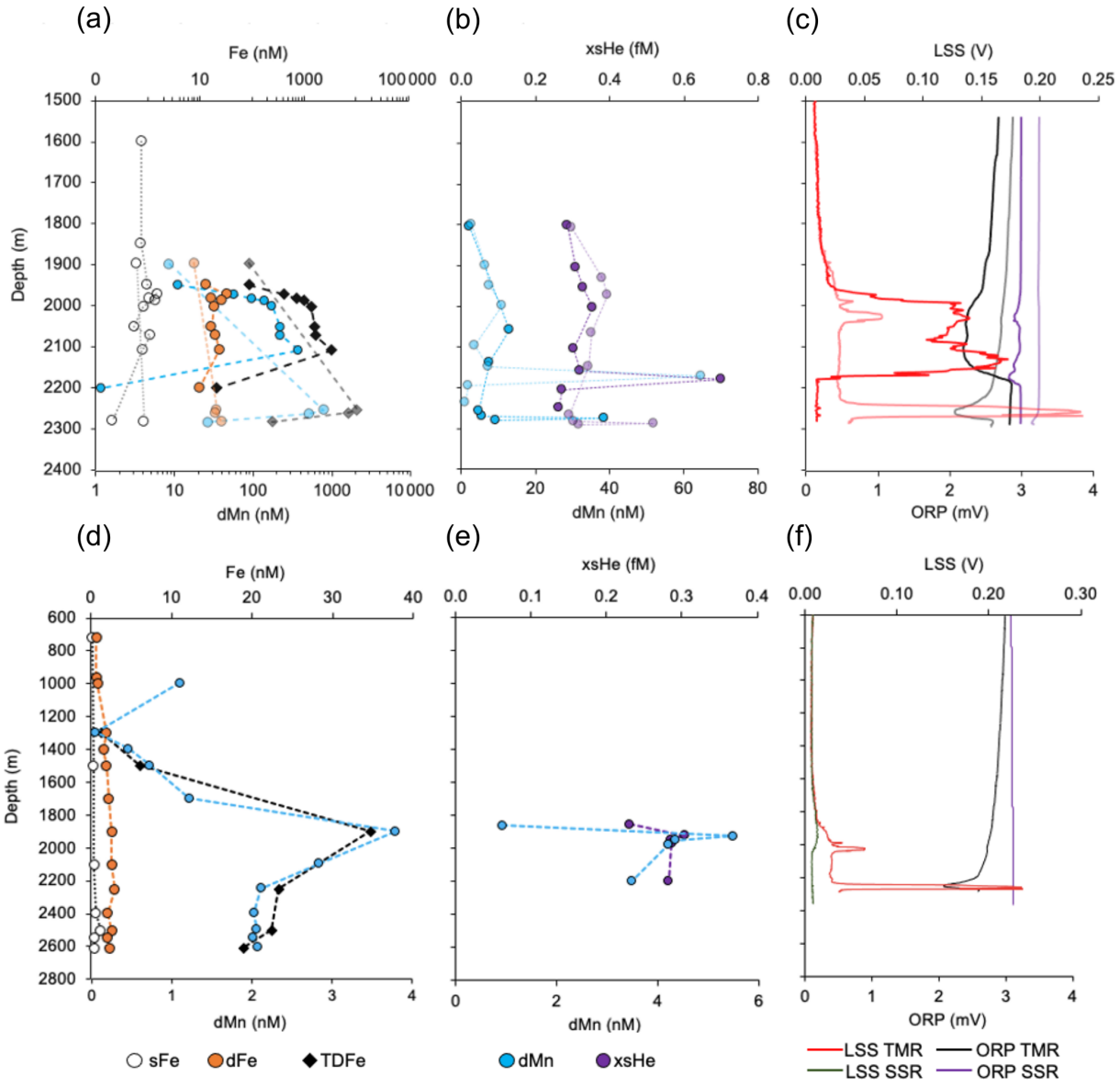

Figure 3. (a) Depth profiles of Fe fractions and dMn over Rainbow (note the log scale on *x* axis) from two separate trace metal clean (TMR) casts. **(b)** dMn and xs^3He from two separate standard rosette (SSR) casts, and light scattering (LSS) and oxidation reduction potential (ORP) sensor profiles for the casts shown in **(a)** and **(b)**. There was no LSS sensor on the standard rosette for casts over Rainbow. The same profiles are shown **(d–f)** for the station 34 km north of Rainbow.

pious amounts of sample water, which would leave limited water available from the trace metal clean rosette to sample for trace metal concentrations, their isotopes and chemical speciation (samples collected during GA13 that will be discussed in future publications). Given the complex physical dynamics of a dispersing plume within a ridge valley (Vic et al., 2018; Lahaye et al., 2019), sampling the same point in the plume twice is nearly impossible. Here we apply the following three different ways of calculating dFe/xs^3He to assess which best represent the plume:

1. *Plume integration method.* Integrate dFe and xs^3He data across the plume depth for samples taken from each cast (e.g. trace metal clean and standard rosette) (Resing et al., 2015; Fitzsimmons et al., 2017). This approach assumes that multiple depths through the plume have been sampled on both casts and are representative of a vertical cross-section of the plume. In a sampling scenario such as that shown in Fig. 2 the plume integration approach is likely to lead to unrealistic dFe/xs^3He ratios and is more suited to an off-axis setting where the plume position is less variable.

Table 2. Summary of plume dFe/xs^{3}He ratios over vent sites and for repeat sampling at TAG and Rainbow using different methods to calculate dFe/xs^{3}He.

	Plume integrated dFe/xs^{3}He (nmol fmol^{-1}) values		Number of samples used in integration	
Vent site (station number)	Integrated from separate casts (method 1)	Dual-Mn method (method 2)	[SR][TMR] Sample depths integrated (n) (method 1)[a]	[TMR] Sample depths integrated (n) (method 2)
Menez Gwen (6)	5.35	11.8	[4][3]	[5]
Lucky Strike (7)	25.8	4.17	[5][4]	[7]
Lucky Strike (8)	ND	7.92	–	[12]
Rainbow (16)	48.6	12.3	[6][9]	[9]
Rainbow (38)	35.5	43.6	[6][3]	[3]
Rainbow[b] (38)	63.0	4.39	[3][2]	[2]
TAG (34)	4.36	7.37	[16][11]	[12]
TAG (35)	87.0	85.6	[17][11]	[15]
TAG (37)	ND	3.60	–	[15]

ND denotes no data, either no dMn data available from the trace metal rosette or no ^{3}He data available from the standard rosette at the equivalent depth. The concentration depth profiles used for the integration at each station are shown in the supplementary figures.
[a] Note that the number of samples captured within the plume differs between the SR and TMR casts because a different number of samples were taken at different depths. [b] The young rising plume was identified over Rainbow close to the seafloor with density lower than that of other stations at the same depth (supplementary information, Figs. S8 and S10 in the Supplement). This signal is separated as these samples will be from a cross-section of the young rising plume as the CTD rosette passed through it. An extended version of this table with data from all stations is presented in the supplementary information (Table S1).

2. *Dual-Mn method.* Constrain the xs^{3}He corresponding to the dFe data using measurements of dMn on both rosette systems. This approach relies on the conservative behaviour of dMn over timescales of weeks (Cowen et al., 1986; Lough et al., 2017, 2019a) (Fig. S2 in the Supplement) and uses the linear relationship between dMn/xs^{3}He measured from the standard rosette (Fig. 4a) to extrapolate the expected xs^{3}He for samples taken with the trace metal clean rosette. The dMn derived xs^{3}He values can then be integrated across the same sample depths as for dFe, which would account for between cast variability in the plume dynamics in a consistent manner. Furthermore, using a site-specific approach helps us to account for any variability in background xs^{3}He present in North Atlantic water masses, where decay of tritium from historic nuclear bomb tests has added ^{3}He (Jenkins et al., 2015b).

3. *xs^{3}He interpolation method.* A third method of estimation was explored using the depth profile of xs^{3}He on the standard rosette and interpolating between depths, to calculate xs^{3}He at the depths sampled by the trace metal clean rosette. This is similar to the approach used by Saito et al. (2013), however the xs^{3}He interpolation method gave significantly different results from the other two methods, generating negative numbers in some instances (Table S1 in the Supplement). The xs^{3}He interpolation method relies on the assumption that the xs^{3}He depth profile is the same on both sampling casts. While the assumption that the shape of the depth concentration profiles is unchanging between casts is likely safe in an off-axis setting, Figs. 3 and S4 in the Supplement show that this assumption cannot be applied within the ridge valley. We therefore focus on the integration methods explained above.

Any samples with xs^{3}He < 0.1 fM, dFe < 0.5 nM, dMn < 0.15 nM and neutral density ≤ 27 kg m^{-3} were excluded from analysis as these waters are deemed to have not been influenced by hydrothermal activity. These background values were selected based on the N. Atlantic values of waters at the same depth range to that of the plume anomalies in this study but from the GEOTRACES Equatorial Atlantic (GA03) and western Atlantic (GA02) at open ocean stations away from any margin sources. Profiles shown in Fig. 3 and the Supplement only show samples characterised as plume samples, i.e. having concentrations greater than that of typical N. Atlantic seawater at the same depth which are included in this analysis. The full data set can be viewed or downloaded through the GEOTRACES international data product (Schlitzer et al., 2018).

Directly over the TAG and Rainbow sites, where the plume was sampled repeatedly, the range of dFe/xs^{3}He across the integration methods was extensive, ranging from 4 to 87 at TAG and 4 to 63 nmol fmol^{-1} at Rainbow (Table 2). Integrated values were different even when the two methods are applied to data from the same casts. The differences in integrated values between casts at the same site is likely to be due to the casts intersecting different areas of the plume (i.e. margins or core) during sampling and/or changes in plume depth over time (time between standard and trace metal clean casts was 2–9 h) (Figs. 2 and 3). The degree of dFe/xs^{3}He variability between integration methods was also observed in the single station estimates from the Menez Gwen and

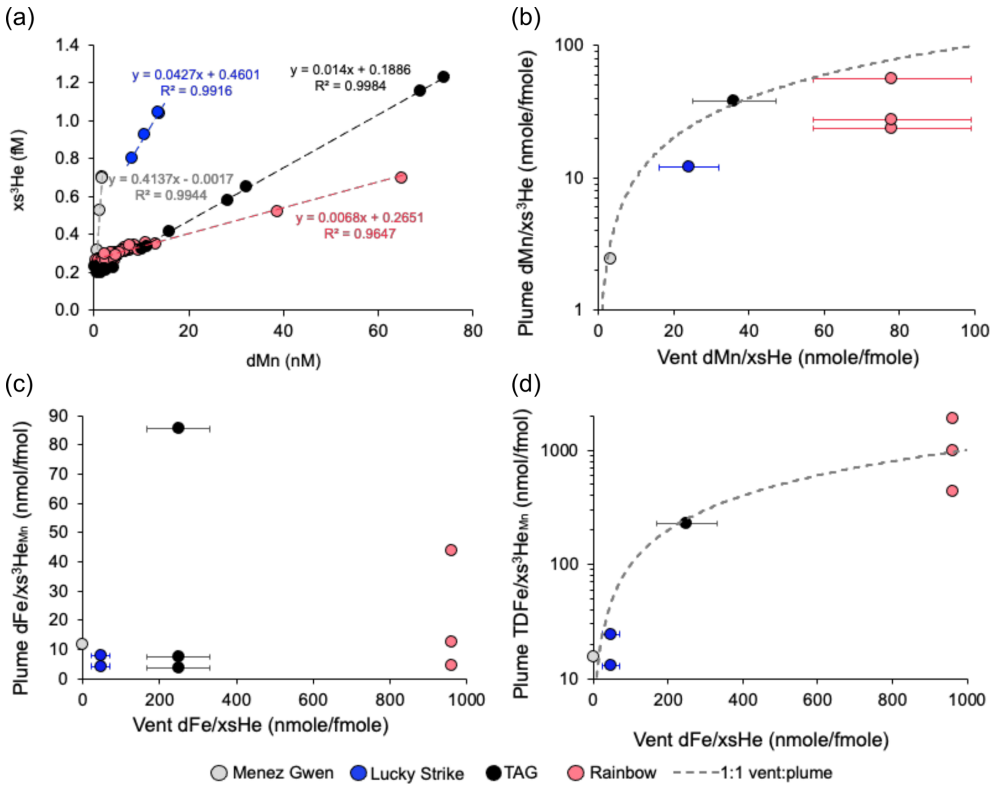

Figure 4. **(a)** Linear relationships between plume dMn and xs^{3}He at sites within 40 km of each vent source from the standard rosette. **(b)** The data from **(a)** is depth integrated to compare the plume dMn/xs^{3}He with vent dMn/xs^{3}He. **(c)** Plume dFe/xs^{3}He$_{Mn}$ (with xs^{3}He derived from dMn) and **(d)** TDFe/xs^{3}He$_{Mn}$ at each vent site station plotted against vent endmember fluid values. Note the logarithmic *y* axis on **(b)** and **(d)** to make it easier to see the position of the points. The grey dashed line **(b, d)** shows a ratio of 1 : 1 where plume ratios are equal to vent ratios. Error bars represent the standard deviation of the average endmembers taken from multiple individual vents at each site (Table 1). Vent xs^{3}He data are from (Jean-Baptiste et al., 2004) and Fe concentration data from Beaulieu et al. (2013) and Findlay et al. (2015) for TAG ($n = 6$) and Rainbow ($n = 3$), Chavagnac et al. (2018) and Pester et al. (2012) for Lucky Strike (average $n = 26$) and Koschinsky et al. (2020) Beaulieu et al. (2013) for Menez Gwen (average $n = 10$).

Lucky Strike locations, where ratios were 5 to 12 and 4 to 26 nmol fmol^{-1}, respectively (Table 2), highlighting the different values that can be produced just by using a different method of calculating dFe/xs^{3}He. The difference in calculated dFe/xs^{3}He ratios was consistently lower (maximum difference of 7 nmol fmol^{-1}) at stations away from the main vent sites (Table S1). Hence, the variability in calculated dFe/xs^{3}He directly over the vent sites is largely down to the changing position of the plume over the vent site relative to the sampling rosette between casts, despite the ship maintaining the same position (Fig. 2).

We focus on the dual-Mn method as the most robust means to estimate the dFe/xs^{3}He ratio. As it can account for differences in position of the plume between sampling devices (Figs. 2 and 3) and background xs^{3}He. Applying site-specific dMn/xs^{3}He relationships from the standard rosette system to the dMn of the TMR rosette, the dual-Mn method finds dFe/xs^{3}He ratios of 12, 4–8, 4–44 and 4–86 nmol fmol^{-1} at Menez Gwen, Lucky Strike, Rainbow and TAG, respectively, for the hydrothermal plumes' directly over these vent sites (Table 2, Fig. 4c). Although the dual-Mn method is less sensitive to differences between casts at the same site, large differences in dFe/xs^{3}He remain over each vent site, with dFe/xs^{3}He still differing by a factor of 2–21 when comparing different casts. The results shown in Table 2. highlight the practical challenges of determining site-specific Fe/xs^{3}He ratios, even in a focused study effort, as a result of complex bottom currents frequently shifting plume waters (Lahaye et al., 2019).

3.2 Linking water column Fe/xs^{3}He ratios to vent fluid endmembers

The extent to which sample depths over the vent sites are representative of the core of the hydrothermal plume can be appraised by (1) assessing LSS and ORP sensor profiles, (2) comparing plume dMn and xs^{3}He from the standard rosette (Fig. 3) and (3) comparing TDFe to xs^{3}He from the trace metal clean rosette (estimated from the dual-Mn method) with the respective vent fluid endmember ratios

(Fig. 4). The vent fluid endmember dFe represents the majority of Fe released from the vent source because vent fluids have a low pH < 2 and significant quantities of particulates are yet to form. In the neutrally buoyant plume emplaced directly over each vent site, Fe removal by particle settling should be in the range of $\sim 0\,\%$–$30\,\%$ Fe endmember vent fluid values and $\sim 0\,\%$ of the Mn (Mottl and McConachy, 1990; Severmann et al., 2004; Findlay et al., 2015; Lough et al., 2019a).

The majority of Fe bearing particles in the unfiltered TDFe samples will be Fe-oxyhydroxides that will dissolve at pH 1.8 after > 1 year storage. A possible exception being that a fraction of the particulates will be FeS_2 which may not dissolve with the addition of HCl (German et al., 1991; Gartman et al., 2014). Extrapolation of experimental data of FeS_2 oxidation rates in seawater and acidic solution (Gartman and Luther, 2014; Constantin and Chiriţă, 2013) indicate that 80 %–100 % of any FeS_2 present in our samples should have oxidised during the ~ 1 year between sampling and analysis. We anticipate that any FeS_2 present in our samples dissolved during sample storage and is included in our measured dFe concentrations and we do not need to be concerned about sample artefacts as a result of FeS_2 nanoparticles.

The plume TDFe/xs^3He and dMn/xs^3He ratios can be compared to vent dFe/xs^3He and dMn/xs^3He ratios, to examine whether the samples from a given cast capture the full extent of the plume rather than just the margins. TDFe/xs^3He_{Mn} and dMn/xs^3He values less than vent fluid values would indicate rapid particle formation and settling has removed Fe and/or Mn from the early plume. The similarity between vent dFe/xs^3He and plume TDFe/xs^3He_{Mn} at 0 km indicates minimal Fe has been lost from particle settling in the immediate plume over each vent site and that the plume cores were indeed sampled from the trace metal rosette (Fig. 4d). Similar results are apparent when comparing vent dMn/xs^3He and plume dMn/xs^3He from the standard rosette (Fig. 4b). One station at Rainbow shows TDFe/xs^3He_{Mn} higher than the 1 : 1 vent plume ratio (Fig. 4d); however, this plume signal was located within 50 m of vents on the seafloor (2300 m) and therefore likely represents the narrow (usually < 1 to several metres wide) buoyant rising plume (see Table 1 caption and Fig. S8). The TDFe/xs^3He_{Mn} value higher than the 1 : 1 line is likely the result of resuspended benthic Fe entrained in the rising plume near the seafloor elevating the TDFe/xs^3He_{Mn} to values higher than the vent dFe/xs^3He. Alternatively, the range of TDFe/xs^3He at the different sites may represent the combined uncertainty from the dual-Mn integration method.

Values of plume dMn/xs^3He fall marginally below the 1 : 1 ratio line for Lucky Strike and Rainbow (Fig. 4b) and could be a result of lower sampling resolution on the standard rosette (Figs. S3 and S4 in the Supplement), uncertainties associated with the plume integration, uncertainties associated with vent fluid endmembers or enhanced removal of dMn by particulates at Lucky Strike and Rainbow. In the case of Rainbow, dMn/xs^3He lower than 1 : 1 could be the result of a higher particulate Fe-oxyhydroxide concentrations in the plume due to the significantly higher Fe/H_2S ratio of the vent fluids ($Fe/H_2S = 26$); however, for Lucky Strike particle removal is less likely to explain dMn/xs^3He lower than 1 : 1 as Lucky Strike vent Fe/H_2S is lower ($Fe/H_2S = 0.18$) and sulfide concentrations are enough to potentially consume all the Fe.

All vents on the North Mid-Atlantic Ridge have similar endmember xs^3He concentrations (18 ± 6 pmol kg^{-1}, $n = 4$ vents (Jean-Baptiste et al., 2004), Table 1). Therefore, differences in vent dFe/xs^3He are solely driven by differences in Fe concentration, which range from 16 to 24 100 µmol kg^{-1} across the four vent sites (Beaulieu et al., 2013; Chavagnac et al., 2018; Koschinsky et al., 2020) determined by the geochemistry of each vent site (Table 1). The endmember vent fluids at Rainbow have the highest dFe/xs^3He (964 nmol fmol^{-1} at Rainbow in contrast to 278 nmol fmol^{-1} at TAG) as the higher temperature, higher Cl^- and low pH of fluids leach more Fe (along with other metals and rare earth elements) from the host rock in comparison to fluids circulating through the sites with basaltic rocks (Douville et al., 2002). Therefore, between-site differences in the plume dFe/xs^3He_{Mn} are not simply related to the vent fluid endmember dFe/xs^3He ratio of each vent. For instance, the highest dFe/xs^3He_{Mn} plume ratio was observed over TAG (86 nmol fmol^{-1}), which was double that of the highest dFe/xs^3He_{Mn} ratio over Rainbow (44 nmol fmol^{-1}) (Table 1, Fig. 4c), despite the five-fold greater Fe content of Rainbow fluids. In contrast, the TDFe/xs^3He_{Mn} values were correlated with the vent fluid endmembers across our sites (Fig. 4d).

3.3 Dissolved–particulate dynamics around the Rainbow and TAG sites

At the 10–40 km sampling distance, a decrease in the Fe/xs^3He_{Mn} ratio was seen across both the total and dissolved Fe size fractions, relative to the maximum ratios sampled over the vent sites (Fig. 5). We interpret this as a difference in plume age between samples taken over the vent site and samples taken in the 10–40 km range, where plume waters are older in the 10–40 km range (therefore more dilution of the vent fluid by seawater) and there has been more time for Fe to precipitate and be removed from the water column. Within 40 km of both the Rainbow and TAG sites, TDFe/xs^3He_{Mn} decreased significantly from the values over the vent site and those of the vent fluids. By comparing the average TDFe/xs^3He_{Mn} of the 10–40 km stations with the dFe/xs^3He of the vent fluids, the amount of vent-derived dFe that has been removed by formation and settling of particles can be estimated for the 0–10 km zone around the vents. Calculated endmember vent Fe losses within the 0–10 km range are $\sim 94\,\%$ for Rainbow and $\sim 83\,\%$ for TAG. The dFe/xs^3He_{Mn} ratios of the 10–40 km sites decreased to be-

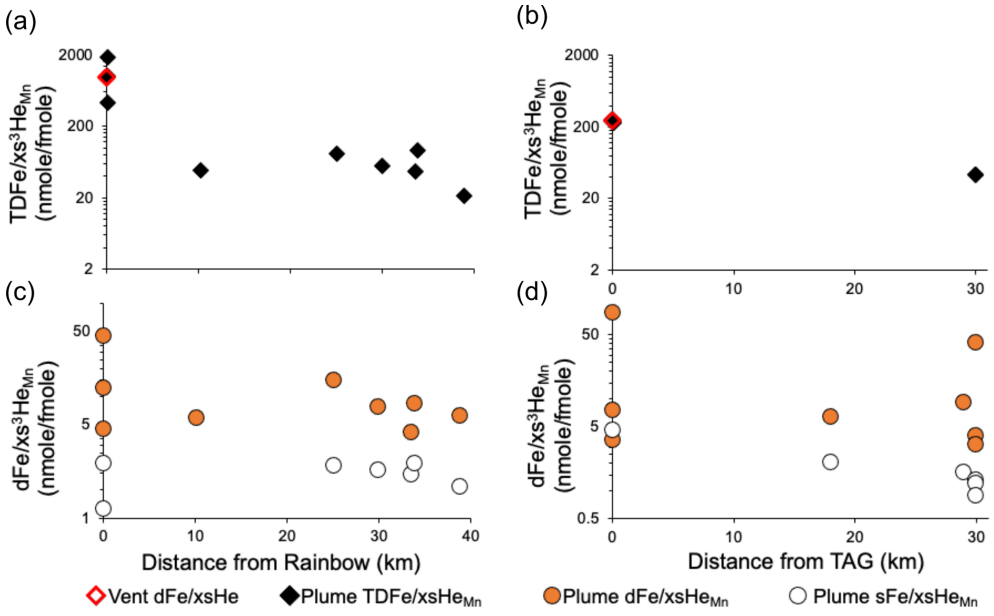

Figure 5. **(a)** Plume TDFe/xs^{3}He$_{Mn}$ with distance (within 40 km) from Rainbow and TAG (within 30 km). **(b)** Change in plume dFe/xs^{3}He$_{Mn}$ and **(c)** sFe/xs^{3}He$_{Mn}$ at Rainbow and **(d)** TAG. Note the log scales on *y* axis.

tween 4 and 15 nmol fmol^{-1} (except for one station 30 km west of TAG which had a ratio of 38 nmol fmol^{-1}, Fig. 5d) in comparison to maximum values over the vent sites at 0 km. The difference between vent fluid dFe/xs^{3}He and plume dFe/xs^{3}He$_{Mn}$ at the 10–40 km range indicates the importance of Fe removal by precipitation of particulates and the subsequent settling of large and/or heavy particulates within 0–10 km of the vent source at both sites, on timescales of days to weeks, leading to a smaller range of dFe/xs^{3}He$_{Mn}$ that may represent broader transport to the ocean interior.

It is particularly notable that despite the TDFe concentrations at Rainbow being an order of magnitude greater than those at TAG (Figs. 5 and 4d), the dFe/xs^{3}He$_{Mn}$ and sFe/xs^{3}He$_{Mn}$ values within 40 km are very similar. One exception is station 30, located ∼ 30 km west of TAG, where a dFe/xs^{3}He$_{Mn}$ of 38 nmol fmol^{-1} is consistent with a younger plume signal with less time for particle formation and settling (Table S1). It is unlikely that there is a new hydrothermal source adding additional Fe to this region west of TAG, given how extensively the area around TAG has been surveyed (Kinoshita et al., 1998). Experimental data examining the oxidation kinetics of Fe at station 30 west of TAG found anomalous rate constants for Fe^{2+}oxidation (log$K$ values), possibly as a result of interactions with organic matter (González-Santana et al., 2021). Anomalous Fe^{2+} oxidation rate constants likely relate to the anomalously high dFe/xs^{3}He$_{Mn}$ at station 30, however we are unable to explain why this site would have higher concentrations of organic matter or why dFe would interact differently with organic matter at this station compared to the other sites.

The average cFe/dFe ratio of the TAG plume (0.82 ± 0.12, $n = 6$) is similar to the Rainbow plume (0.84 ± 0.10, $n = 7$), indicating that dFe is predominantly colloidal within 40 km of the vent source at both sites, with little change over these distances (Fig. 6a). In contrast, there is a clear difference in the appPFe/dFe ratio (Fig. 6b), which is elevated in the Rainbow plume and consistent with the higher concentration Fe source at Rainbow. The difference in the appPFe/dFe ratio between Rainbow and TAG highlights a substantially larger role for dissolved–particulate interactions at the Rainbow site, relative to TAG. It is due to these strong particulate–dissolved exchanges that the dFe/xs^{3}He$_{Mn}$ ratios 40 km from source are largely similar for both TAG and Rainbow, despite the Rainbow neutrally buoyant plume having initially half the dFe/xs^{3}He over the vent site (44 nmol fmol^{-1}) relative to TAG (86 nmol fmol^{-1}) (Fig. 5c and d). If dFe was behaving entirely conservatively, we would anticipate the range of dFe/xs^{3}He at the 10–40 km stations around Rainbow (4–15 nmol fmol^{-1}) to be lower than that of the equivalent sites around TAG (4–9 fmol nmol^{-1}, excluding the anomalous western station). The similarity in dFe/xs^{3}He at 10–40 km suggests the dFe/xs^{3}He ratio in the Rainbow plume was buffered by disaggregating or dissolving particles. Specifically, particles which were too large to initially be part of the dissolved phase (> 0.2 µm) but not large or dense enough to form particles that rapidly settle out of the plume within the 40 km sampling area.

Separating whether particle disaggregation or dissolution is the driving mechanism behind the buffering of dFe concentrations between the 0 and 40 km stations at Rainbow is difficult from these results. We would anticipate particle dis-

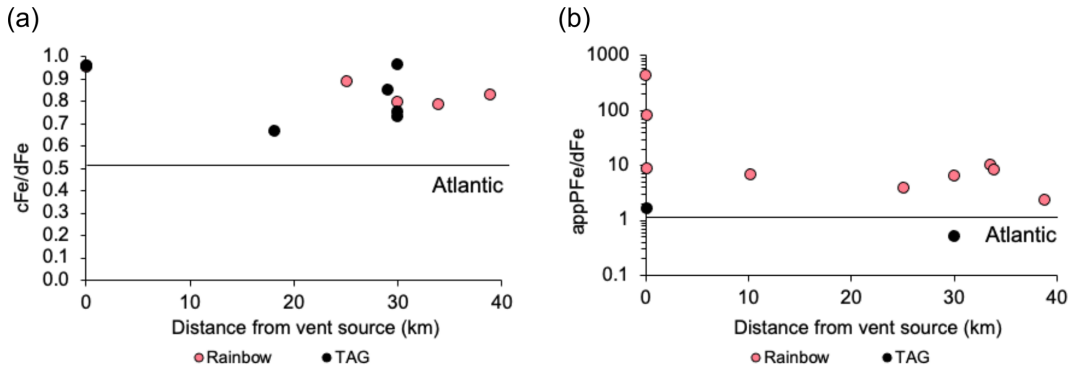

Figure 6. (a) Change in integrated cFe/dFe (where cFe = dFe − sFe) and **(b)** appPFe/dFe of the plume with distance from Rainbow and TAG where appPFe = TDFe − dFe. Note the log scale on the *y* axis of **(b)**. Solid black lines show the same ratios for open Atlantic deep waters taken from Milne et al. (2017) for appPFe/dFe and Kunde et al. (2019b) for cFe/dFe.

solution would transfer appPFe to the sFe fraction as aqueous ions, causing a shift in the cFe/dFe ratio (Fig. 6) and we did not observe this. Therefore, we deem it more likely that dFe/xs^{3}He at 10–40 km range is buffered by disaggregation of appPFe particles rather than dissolution, or there is dissolution followed by rapid re-precipitation as inorganic colloidal Fe or immediate binding to colloidal sized Fe ligands.

4 Wider implications

Our results do not show constant linear trends between dFe and xs^{3}He (Fig. 5) that have been observed over larger distances in basin-scale sampling efforts in the Pacific (Resing et al., 2015). As well as looking at integrated values, we examined the correlation between xs^{3}He$_{Mn}$ and dFe across individual samples and found r^2 values of 0.956 to 0.811 for Lucky Strike and Menez Gwen, and 0.442 and 0.587 for Rainbow and TAG, respectively (Fig. S11 in the Supplement). Interestingly, sites like TAG and Rainbow with higher particle concentrations had lower r^2 values. These deviations from linear relationships likely indicate ongoing particulate–dissolved Fe exchange at the 0–10 km scale, which has been observed previously at smaller scale sampling resolution (Lough et al., 2019a).

The large differences in appPFe-dFe dynamics over 10's of km between the TAG and Rainbow plumes highlight the potential importance of particulate–dissolved Fe exchange in governing hydrothermal Fe transport from distinct vent sources. If particulate Fe concentrations extend the longevity of hydrothermal Fe in the deep ocean as hypothesised (Fitzsimmons et al., 2017), then it is likely that the residence time of hydrothermal Fe will depend on the amount of Fe released from vents on the seafloor and the presence of ligands to facilitate particulate–dissolved Fe exchange. In the particle exchange conceptual model, we would anticipate the residence time of dFe in the Rainbow plume to be longer than the TAG plume, due to higher particulate Fe concentrations facilitating transport over longer distances. Alternatively, if hydrothermal dFe behaves conservatively (Resing et al., 2015) (and dissolved–particulate Fe exchange is negligible), then the longevity of hydrothermal Fe will depend on how much Fe forms colloidal and soluble phases in the early stages of the plume. In the conservative colloids framework, we would anticipate dFe in the TAG plume to have a longer residence time in the water column due to initially higher dFe/xs^{3}He (Fig. 4c and Table 1). In both conceptual models, Fe-binding ligands are likely to play a key role by either facilitating particulate–dissolved Fe exchange or by stabilising dFe species. However, if the formation of colloids in the first several metres of plume rise is largely a result of inorganic precipitation of dFe, then the role of ligands will be less important in the conservative colloids model. The "conservative Fe colloids" model has been tested in global biogeochemical models (Resing et al., 2015) and estimates a global hydrothermal Fe flux of 4 ± 1 Gmol yr^{-1}. A version of the "particulate–dissolved Fe exchange" model has also been tested and this produces a much lower flux estimate of 0.12 ± 0.07 Gmol yr^{-1} (Roshan et al., 2020). Refining these models and deciding which is closer to the truth requires experimental data on the rate of particulate–dissolved Fe exchange and stability of colloidal phases in both hydrothermal plumes and the deep ocean.

4.1 What controls ridge axis dissolved Fe to helium ratios?

Given the significantly higher vent fluid dFe/xs^{3}He at Rainbow compared with TAG (Table 1), the dFe/xs^{3}He at distances 10 to 40 km from the vent sites is remarkably similar (8 ± 4 versus 12 ± 14 nmol fmol^{-1}, respectively, $n = 5$). The similarity in dFe/xs^{3}He at the 10–40 km range between Rainbow and TAG would suggest there is a cap on the amount of vent fluid dFe that can be converted into dFe in the plume, which is possibly the result of similar Fe-binding

ligand concentrations and/or strength at both sites. Ligands could be sourced from weakly binding pervasive background Fe-binding ligands present in deep ocean waters or Fe-binding ligands sourced locally from the ecosystems of both vents present at similar concentrations and binding strengths (Kleint et al., 2016). Alternatively, Fe^{2+} oxidation rates may determine the extent to which Fe is separated between dissolved and particulate phases and hence the dFe/xs^{3}He ratio. Rates of Fe^{2+} oxidation measured at both these sites show a similar range of Fe^{2+} half-lives in the plumes (TAG = 1–130 min, Rainbow = 20–160 min; González-Santana et al., 2021). The initial concentration of Fe released from Rainbow vents is 5 times higher than at TAG, despite a similar He concentration, and if Fe^{2+} oxidation rates were the main driver of dFe concentrations, the Rainbow plume should have higher ratios of dFe/xs^{3}He. This contrasts with our observations, suggesting that Fe^{2+} oxidation rates are less important in establishing plume dFe/xs^{3}He at scales of 10's of km than ligand strength, concentration or inorganic colloid formation.

Vent fluids with molar $Fe/H_2S < 1$ are likely to precipitate higher concentrations of FeS_2 nanoparticles in plumes (Gartman et al., 2014). Given that TAG has a lower Fe/H_2S ratio than Rainbow (Fe/H_2S is 1 mmol mmol^{-1} for TAG vents and 26 mmol mmol^{-1} for Rainbow; Table 1), we should anticipate a higher concentration of FeS_2 nanoparticles in the TAG plume. Higher concentrations of FeS_2 nanoparticles may offer an explanation as to why the maximum dFe/xs^{3}He of the TAG plume (86 fmol nmol^{-1}) was high in comparison to Rainbow (44 fmol nmol^{-1}). The twofold difference in maximum plume dFe/xs^{3}He between TAG and Rainbow is small compared to the 18-fold difference in vent fluid Fe/H_2S (Table 1), and based on the observed trend between FeS_2 nanoparticle concentration and Fe/H_2S shown in Gartman et al. (2014), we would only anticipate an additional 4 % FeS_2 concentration in the dissolved phase at TAG. This suggests that the formation of FeS_2 nanoparticles in the nascent plume cannot fully explain differences in plume dFe/xs^{3}He between sites. From our comparison, it would seem that for vent sites located along the same ridge, ligand concentration and strength are likely to be a more important control on dFe/xs^{3}He over the ridge axis than vent fluid chemistry and Fe^{2+} oxidation rate (set by water column O_2 and pH; Santana-Casiano et al., 2000; Millero et al., 1987).

4.2 Particle plumes escaping the mid-ocean ridge valley

If we only consider the dFe flux from plumes, excluding any contribution from particulates, site-to-site differences in the chemistry of hydrothermal systems give a range of 8–12 nmol fmol^{-1} (averages from Rainbow and TAG at 10–40 km) for dFe/xs^{3}He within the ridge valley (Fig. 5). Therefore, any subsequent dFe flux calculated based on dFe/xs^{3}He will only vary by a similar magnitude. This would mean that current biogeochemical models using a global dFe/xs^{3}He ratio of 10 nmol fmol^{-1} (within the 8–12 nmol fmol^{-1} range observed at 10–50 km) are using a reasonably well-defined input flux of "dissolved" hydrothermal Fe into the deep ocean. However, given the differences between sites in appFe/dFe (Fig. 6), we need to consider the impact of particulate Fe on the hydrothermal Fe flux and how this may vary across the global ocean ridge crest. Models of hydrothermal Fe fluxes are calculated based on a fixed dFe/xs^{3}He value, estimating dFe flux based on xs^{3}He fluxes which vary with ridge spreading rate. We found no indication of a relationship between vent endmember and plume dFe/xs^{3}He over each vent site, however we did find a relationship between TDFe/xs^{3}He and the vent endmember (Fig. 4), suggesting this parameter may be more relevant for linking the Fe flux from vents with xs^{3}He fluxes from ridges. Fine-grained suspended particulates maintain TDFe/xsHe above dFe/xs^{3}He and clearly persist at the 10–40 km range and are likely to be transported beyond the ridge. There is an argument to be made that these fine-grained suspended particles should be represented in the values used to estimate hydrothermal Fe fluxes in global biogeochemical models.

All stations maintain a cFe/dFe ratio greater than open ocean N. Atlantic cFe/dFe values of 0.5 (Fig. 6a). Clearly within the ridge valley, plume waters maintain a higher colloidal Fe load than open ocean N. Atlantic waters. If the residence time of Fe-rich plumes trapped within the Mid-Atlantic Ridge valley are similar to the time it takes Lagrangian particles to exit the ridge valley in dispersion models (Vic et al., 2018), then wherever deep waters escape the ridge valley they may also carry elevated concentrations of particulate and dissolved Fe to the deep Atlantic ocean.

Using Stokes' law, we can calculate if it is reasonable to expect plume waters exiting the ridge valley to carry sufficient colloidal and particulate Fe or whether it will have settled out of the water column to the sediment. Plume waters from Lucky Strike take $\sim$ 30 d to exit the ridge valley based on Lagrangian particle dispersion experiments (Vic et al., 2018). As there are no other comparative dispersion experiments for other sites on the MAR, we can assume that the dispersion time for plume waters to exit the ridge valley is the same for other vents on the MAR as it is at Lucky Strike. The approximate distance from sources of venting at the centre of the valley to the outer ridge flank is $\sim$ 100 km. We can then calculate that an average particle of ferrihydrite 6 µm in size (average of 6 ± 6 µm, $n = 28$, based on published microscopy images, Table S2 in the Supplement; Feely et al., 1994; Breier et al., 2014; Lough et al., 2019b, a, 2017; Toner et al., 2009, 2016; Von Der Heyden et al., 2012) would have settled 87 m through the water column as plume waters travel from the vent source out of the ridge valley. Given the abyssal seafloor depths outside the ridge are $\sim$ 4000 m and neutrally buoyant plume heights along the ridge are in the range of 800–3200 m (Fig. S7 in the Supplement), we can conclude that there is not enough time for the average sized Fe oxyhydroxide particle to reach the seafloor. Settling of

87 m during transport out of the ridge valley is likely still a conservative estimate of settling when we consider that (1) microscopy techniques used to estimate particle diameter will be biased towards observing larger particles that are easier to detect and image, (2) particles are often a mix of Fe oxyhydroxide minerals and organic carbon making them less dense than pure ferrihydrite (Toner et al., 2009; Yucel et al., 2011; Gartman et al., 2014; Lough et al., 2017; Hoffman et al., 2018; Lough et al., 2019b; Lough et al., 2019a), and (3) Lagrangian particles in dispersion models are carried ~ 100 m vertically beyond the neutrally buoyant plume depth by turbulent mixing across the ridge (Vic et al., 2018) and tidal forces can shift neutrally buoyant plume depths by ~ 100 m within the ridge valley (Jean-Baptiste et al., 2004). Therefore, physical mixing processes should counteract the effects of particle settling and we see some evidence of this in Fig. 3 where the maximum concentration of elements is at a shallower depth (~ 1900 m) at stations away from the vent source (Fig. 3d and e) in comparison to stations over the vents (2000–2300 m, Fig. 3a and b). It is therefore likely that the TDFe concentrations we observe within 10–40 km of the vents will be similar to those of waters exiting the ridge valley and entering the deep ocean with the majority of fast particulate Fe removal to sediments happening within 10 km of the vent site (i.e. timescale of days, particles > 30 µm in diameter that are exclusively Fe oxyhydroxide or Fe sulfide minerals).

For slow spreading mid-ocean ridges (i.e. ridges with a substantially deep ridge valley), we should conceptualise them as "leaky ridges" rather than individual "leaky vents" in order to fully understand their impact of the deep ocean Fe budget. As it is the point at which plume waters exit the ridge valley, the Fe carrying capacity of these waters (particulates and dissolved phase) and the rate at which Fe is removed from the plume as settling particles are key to determining the impact of hydrothermal vents on deep ocean Fe concentrations. The extent to which Fe is removed from the plume before exiting the ridge valley is dependent on the time it takes from plume waters to be transported and diluted, making particle collisions and therefore aggregation less likely. Hence understanding the physical mixing regimes of waters moving through ridge valleys is of key importance to further constraining hydrothermal Fe fluxes, especially for slow spreading ridges where plumes will initially be topographically constrained. Focusing research efforts on understanding changes in Fe concentrations within physical mixing regimes will provide an improved ability to understand Fe removal from hydrothermal plumes with transport away from vent sources, in comparison to assessing Fe removal within the context of the path of a ship across the ocean (Nishioka et al., 2013; Saito et al., 2013; Resing et al., 2015; Fitzsimmons et al., 2017).

It is possible for global biogeochemical models to overestimate Fe fluxes from some mid-ocean ridges, as the complex mesoscale mixing regimes through ridge valleys are not parameterised at the global scale. In order for this to be the case, the pathways that ridge valley waters travel from the vent source to exiting the ridge valley would have to be significantly longer than those modelled for Lucky Strike (Vic et al., 2018), allowing for an extended period of time for scavenging and precipitation of Fe (resulting in lower dFe/xs^{3}He values than those used in models and observed in this study) leading to lower Fe fluxes. If we lead with our assumption that plume dispersion time at Lucky Strike (Vic et al., 2018) is representative of most plumes emanating from mid-ocean ridges (given that the physical mixing regimes acting on the plume and topographic controls will be similar along the ridge), and that particulates at the 10–40 km distance are likely to remain suspended in the water column or re-dissolve, then using TDFe/xs^{3}He ratios of 55 ± 24 $n = 7$ (average all TAG and Rainbow stations at 10–40 km distance) in biogeochemical models may be more representative of the hydrothermal Fe flux which is $5\times$ greater than the ratio of 10 used currently (Tagliabue et al., 2010; Resing et al., 2015).

4.3 Future work

Similar process studies that sample plumes from vents with different geochemistry along a ridge will be needed to test the ideas discussed here further. Specifically focusing on the dispersion of plumes through the ridge valley walls and whether there is any difference in Fe-binding ligand strength or concentration between vent sites with different amounts of diffuse flow that likely act as a source of ligands. Our findings from the comparison of TAG and Rainbow show that the inorganic geochemistry of individual vents sites plays a minor role in dictating the near-field plume dFe concentration; however, an excess of plume pFe resulting from higher vent fluid Fe concentrations may support dFe longevity via dFe–pFe exchange, provided the particulates remain suspended, disaggregate or re-dissolve in the water column. It is therefore possible that vents situated in an ultramafic setting (i.e. low pH and high Cl^- content due to interaction with ultramafic rocks during hydrothermal circulation) may provide more Fe to the deep ocean in comparison to basalt hosted systems. However, constraining the full impact of ultramafic vent sites on the net global hydrothermal Fe flux requires more knowledge about the frequency of their occurrence along the global ridge crest (Baker et al., 2016).

To improve our estimates of how much hydrothermal Fe fertilises surface ocean productivity, we need further information on the location and frequency of vent systems along the global ridge crest, how much variability there is in the hydrothermal ligand source between vent sites, what controls the rate of particulate dissolved exchange in the plume and how rapidly hydrothermal Fe is scavenged from the deep ocean.

5 Conclusions

Our results show that care must be taken when extrapolating Fe/xs^{3}He results from ocean survey sampling, e.g. as part of GEOTRACES. This is due to uncertainties associated with the at-sea sampling strategy and the temporal nature of plume dynamics that can yield significant variability in Fe/xs^{3}He ratios. We recommend that measurements of dMn across different casts at the same site are a useful means by which to minimise sampling uncertainties, especially when combined with ORP and LSS sensors to target plume sampling across different deployments. We show that when dMn and xs^{3}He measurements are used alongside both dFe and TDFe observations, it is possible to link the observed plume dynamics to vent fluid endmembers and determine the important dissolved–particulate dynamics that shape the Fe/xs^{3}He signals that integrate at broader spatial scales.

Despite 5× higher concentrations of Fe (but similar xs^{3}He) venting from Rainbow relative to TAG, we observed lower dFe/xs^{3}He in the Rainbow plume over the vent site (Fig. 4c). The additional Fe venting at Rainbow was converted into particulates and this was reflected in the ratio of appPFe/dFe at Rainbow which is higher than TAG (Fig. 6b). These results suggest that there is a threshold placed on the amount of venting dFe that can be converted to plume dFe; we hypothesise that this threshold is set by the concentration of Fe-binding ligands. Greater than 80 % of vent fluid Fe formed large dense particulates that settled rapidly within 10 km's and a smaller but significant fraction remained suspended in the water column. The particulate Fe persisting beyond the 10 km distance may enhance the longevity of plume dFe through particulate–dissolved exchange. The extent of ongoing particulate–dissolved Fe exchange with further plume dispersion will depend on the speciation and size distribution of particulates as well as ligand strength, concentration and longevity which may differ between these two sites. Future work examining any differences in particle speciation and size between these two sites will be better placed to determine whether the higher concentration of suspended particulates at Rainbow will enhance the longevity of the hydrothermal plume relative to the TAG plume.

Data availability. Data in Table 1 from the inter-ridge database were taken from the Vent DB collection (https://doi.org/10.1594/IEDA/100207, Mottl, 2012) via the Earth chem library (https://www.earthchem.org/ecl/). The data from the GA13 transect are available (to view and download) as part of the GEOTRACES international data product which can be accessed online via https://www.egeotraces.org/ (Schlitzer et al., 2018).

Supplement. The supplement related to this article is available online at: https://doi.org/10.5194/bg-20-405-2023-supplement.

Author contributions. AT and MCL wrote the proposal to secure funding for the project. The sampling design for fieldwork was conceived by AT, MCL and JAR. AJML, AT, JAR, NJW and MCL mobilised equipment and consumables for fieldwork. Samples were collected in the field by AJML, AT, JAR and MCL. All sample analysis was conducted by AJML and CD apart from helium analysis which was paid for at Woods Hole Oceanographic Institute. NJW calculated xs^{3}He values. AJML analysed and interpreted the data, produced the figures and wrote the paper. All authors provided comments on subsequent drafts of the paper.

Competing interests. The contact author has declared that neither of the authors has any competing interests.

Disclaimer. Publisher's note: Copernicus Publications remains neutral with regard to jurisdictional claims in published maps and institutional affiliations.

Acknowledgements. We thank Shaun Rigby and Ric Williams for Helium sampling at sea and Bill Jenkins for He analysis. We also thank the captain and crew of the RRS *James Cook* and everyone that contributed to the GA13 sampling effort on board. This is CICOES publication no. 2021-1169 and PMEL no. 5322.

Financial support. This work is part of the FeRidge project (GEOTRACES section GA13) which was supported by the Natural Environment Research Council funding (NERC United Kingdom grant NE/N010396/1 to MCL and NE/N009525/1 to Alessandro Tagliabue). Clément Demasy was additionally funded by the Occitanie / Pyrénées-Méditerranée Regional Council. Joseph A. Resing was funded by the NOAA Ocean Exploration and Earth–Ocean Interactions programs from PMEL and CICOES. The international GEOTRACES programme is possible in part because of support from the US National Science Foundation (grant OCE-1840868) to the Scientific Committee on Oceanic Research (SCOR).

Review statement. This paper was edited by Aninda Mazumdar and reviewed by three anonymous referees.

References

Ardyna, M., Lacour, L., Sergi, S., d'Ovidio, F., Sallée, J.-B., Rembauville, M., Blain, S., Tagliabue, A., Schlitzer, R., Jeandel, C., Arrigo, K. R., and Claustre, H.: Hydrothermal vents trigger massive phytoplankton blooms in the Southern Ocean, Nat. Commun., 10, 2451, https://doi.org/10.1038/s41467-019-09973-6, 2019.

Baker, E. T., Resing, J. A., Haymon, R. M., Tunnicliffe, V., Lavelle, J. W., Martinez, F., Ferrini, V., Walker, S. L., and Nakamura, K.: How many vent fields? New estimates of vent field populations on ocean ridges from precise mapping of hydrother-

mal discharge locations, Earth Planet. Sc. Lett., 449, 186–196, https://doi.org/10.1016/j.epsl.2016.05.031, 2016.

Beaulieu, S. E., Baker, E. T., German, C. R., and Maffei, A.: An authoritative global database for active submarine hydrothermal vent fields [data set], Geochem. Geophy. Geosy., 14, 4892–4905, https://doi.org/10.1002/2013gc004998, 2013.

Bennett, S. A., Achterberg, E. P., Connelly, D. P., Statham, P. J., Fones, G. R., and German, C. R.: The distribution and stabilisation of dissolved Fe in deep-sea hydrothermal plumes, Earth Planet. Sc. Lett., 270, 157–167, https://doi.org/10.1016/j.epsl.2008.01.048, 2008.

Breier, J. A., Sheik, C. S., Gomez-Ibanez, D., Sayre-McCord, R. T., Sanger, R., Rauch, C., Coleman, M., Bennett, S. A., Cron, B. R., Li, M., German, C. R., Toner, B. M., and Dick, G. J.: A large volume particulate and water multi-sampler with in situ preservation for microbial and biogeochemical studies, Deep-Sea Res. Pt. I, 94, 195–206, https://doi.org/10.1016/j.dsr.2014.08.008, 2014.

Chavagnac, V., Leleu, T., Fontaine, F., Cannat, M., Ceuleneer, G., and Castillo, A.: Spatial Variations in Vent Chemistry at the Lucky Strike Hydrothermal Field, Mid-Atlantic Ridge (37° N): Updates for Subseafloor Flow Geometry From the Newly Discovered Capelinhos Vent, Geochem. Geophy. Geosy., 19, 4444–4458, https://doi.org/10.1029/2018gc007765, 2018.

Constantin, C. A. and Chiriţă, P.: Oxidative dissolution of pyrite in acidic media, J. Appl. Electrochem., 43, 659–666, https://doi.org/10.1007/s10800-013-0557-y, 2013.

Cowen, J. P., Massoth, G. J., and Baker, E. T.: Bacterial scavenging of Mn and Fe in a Mid Field to Far Field hydrothermal particle plume, Nature, 322, 169–171, https://doi.org/10.1038/322169a0, 1986.

Cowen, J. P., Massoth, G. J., and Feely, R. A.: Scavenging rates of dissolved manganese in a hydrothermal vent plume, Deep-Sea Res., 37, 1619–1637, https://doi.org/10.1016/0198-0149(90)90065-4, 1990.

Cutter, G., Andersson, P., Codispoti, L., Croot, P., François, R., Lohan, M.C., Obata, H., Rutgers, v. d. L. M.: Sampling and Sample-handling Protocols for GEOTRACES Cruises, in: Michiel.Rutgers.v.d.Loeff (Ed.). EPIC.awi.de, https://epic.awi.de/id/eprint/34484/ (last access: 20 June 2021), 2010.

Douville, E., Charlou, J. L., Oelkers, E. H., Bienvenu, P., Colon, C. F. J., Donval, J. P., Fouquet, Y., Prieur, D., and Appriou, P.: The rainbow vent fluids (36°14′ N, MAR): the influence of ultramafic rocks and phase separation on trace metal content in Mid-Atlantic Ridge hydrothermal fluids, Chem. Geol., 184, 37–48, https://doi.org/10.1016/s0009-2541(01)00351-5, 2002.

Feely, R. A., Gendron, J. F., Baker, E. T., and Lebon, G. T.: Hydrothermal plumes along the east pacific rise, 8°40′ to 11°50′ N: Particle distribution and composition, Earth Planet. Sc. Lett., 128, 19–36, https://doi.org/10.1016/0012-821x(94)90023-x, 1994.

Field, M. P. and Sherrell, R. M.: Dissolved and particulate Fe in a hydrothermal plume at 9°45′ N, East Pacific Rise: Slow Fe(II) oxidation kinetics in Pacific plumes, Geochim. Cosmochim. Ac., 64, 619–628, https://doi.org/10.1016/s0016-7037(99)00333-6, 2000.

Findlay, A. J., Gartman, A., Shaw, T. J., and Luther, G. W.: Trace metal concentration and partitioning in the first 1.5 m of hydrothermal vent plumes along the Mid-Atlantic Ridge: TAG, Snakepit, and Rainbow, Chem. Geol., 412, 117–131, https://doi.org/10.1016/j.chemgeo.2015.07.021, 2015.

Fitzsimmons, J. N., John, S. G., Marsay, C. M., Hoffman, C. L., Nicholas, Sarah L., Toner, B. M., German, C. R., and Sherrell, R. M.: Iron persistence in a distal hydrothermal plume supported by dissolved–particulate exchange, Nat. Geosci., 10, 195, https://doi.org/10.1038/ngeo2900, 2017.

Gartman, A. and Luther, G. W.: Oxidation of synthesized submicron pyrite (FeS2) in seawater, Geochim. Cosmochim. Ac., 144, 96–108, https://doi.org/10.1016/j.gca.2014.08.022, 2014.

Gartman, A., Findlay, A. J., and Luther, G. W.: Nanoparticulate pyrite and other nanoparticles are a widespread component of hydrothermal vent black smoker emissions, Chem. Geol., 366, 32–41, https://doi.org/10.1016/j.chemgeo.2013.12.013, 2014.

German, C. R., Campbell, A. C., and Edmond, J. M.: Hydrothermal scavenging at the Mid-Atlantic Ridge - modification of trace-element dissolved fluxes, Earth Planet. Sc. Lett., 107, 101–114, https://doi.org/10.1016/0012-821x(91)90047-l, 1991.

González-Santana, D., González-Dávila, M., Lohan, M. C., Artigue, L., Planquette, H., Sarthou, G., Tagliabue, A., and Santana-Casiano, J. M.: Variability in iron(II) oxidation kinetics across diverse hydrothermal sites on the northern Mid Atlantic Ridge, Geochim. Cosmochim. Ac., 297, 143–157, https://doi.org/10.1016/j.gca.2021.01.013, 2021.

Gottschalk, J., Battaglia, G., Fischer, H., Frölicher, T. L., Jaccard, S. L., Jeltsch-Thömmes, A., Joos, F., Köhler, P., Meissner, K. J., Menviel, L., Nehrbass-Ahles, C., Schmitt, J., Schmittner, A., Skinner, L. C., and Stocker, T. F.: Mechanisms of millennial-scale atmospheric CO_2 change in numerical model simulations, Quaternary Sci. Rev., 220, 30–74, https://doi.org/10.1016/j.quascirev.2019.05.013, 2019.

Hawkes, J. A., Connelly, D. P., Gledhill, M., and Achterberg, E. P.: The stabilisation and transportation of dissolved iron from high temperature hydrothermal vent systems, Earth Planet. Sc. Lett., 375, 280–290, https://doi.org/10.1016/j.epsl.2013.05.047, 2013.

Hoffman, C. L., Nicholas, S. L., Ohnemus, D. C., Fitzsimmons, J. N., Sherrell, R. M., German, C. R., Heller, M. I., Lee, J.-m., Lam, P. J., and Toner, B. M.: Near-field iron and carbon chemistry of non-buoyant hydrothermal plume particles, Southern East Pacific Rise 15° S, Mar. Chem., https://doi.org/10.1016/j.marchem.2018.01.011, 2018.

James, R. H. and Elderfield, H.: Dissolved and particulate trace metals in hydrothermal plumes at the Mid-Atlantic Ridge, Geophys. Res. Lett., 23, 3499–3502, https://doi.org/10.1029/96gl01588, 1996.

Jean-Baptiste, P., Fourré, E., Charlou, J.-L., German, C. R., and Radford-Knoery, J.: Helium isotopes at the Rainbow hydrothermal site (Mid-Atlantic Ridge, 36°14′ N), Earth Planet. Sc. Lett., 221, 325–335, https://doi.org/10.1016/S0012-821X(04)00094-9, 2004.

Jenkins, W. J., Smethie, W. M., Boyle, E. A., and Cutter, G. A.: Water mass analysis for the U. S. GEOTRACES (GA03) North Atlantic sections, Deep-Sea Res. Pt. II, 116, 6–20, https://doi.org/10.1016/j.dsr2.2014.11.018, 2015a.

Jenkins, W. J., Lott, D. E., Longworth, B. E., Curtice, J. M., and Cahill, K. L.: The distributions of helium isotopes and tritium along the U. S. GEOTRACES North Atlantic sections (GEOTRACES GAO3), Deep-Sea Res. Pt. II, 116, 21–28, https://doi.org/10.1016/j.dsr2.2014.11.017, 2015b.

Jenkins, W. J., Lott, D. E., and Cahill, K. L.: A determination of atmospheric helium, neon, argon, krypton, and xenon solubility concentrations in water and seawater, Mar. Chem., 211, 94–107, https://doi.org/10.1016/j.marchem.2019.03.007, 2019.

Kinoshita, M., Von Herzen, R. P., Matsubayashi, O., and Fujioka, K.: Tidally-driven effluent detected by long-term temperature monitoring at the TAG hydrothermal mound, Mid-Atlantic Ridge, Phys. Earth Planet. In., 108, 143–154, https://doi.org/10.1016/S0031-9201(98)00092-2, 1998.

Kleint, C., Hawkes, J. A., Sander, S. G., and Koschinsky, A.: Voltammetric Investigation Of Hydrothermal Iron Speciation, Frontiers in Marine Science, 3, 75, https://doi.org/10.3389/fmars.2016.00075, 2016.

Koschinsky, A., Schmidt, K., and Garbe-Schönberg, D.: Geochemical time series of hydrothermal fluids from the slow-spreading Mid-Atlantic Ridge: Implications of medium-term stability, Chem. Geol., 552, 119760, https://doi.org/10.1016/j.chemgeo.2020.119760, 2020.

Kunde, K., Wyatt, N. J., Gonzalez-Santana, D., Tagliabue, A., Mahaffey, C., and Lohan, M. C.: Iron Distribution in the Subtropical North Atlantic: The Pivotal Role of Colloidal Iron, Global Biogeochem. Cy., 33, 1532–1547, https://doi.org/10.1029/2019gb006326, 2019a.

Kunde, K., Wyatt, N. J., González-Santana, D., Tagliabue, A., Mahaffey, C., and Lohan, M. C.: Iron Distribution in the Subtropical North Atlantic: The Pivotal Role of Colloidal Iron, Global Biogeochem. Cy., 33, 1532–1547, https://doi.org/10.1029/2019GB006326, 2019b.

Lahaye, N., Gula, J., Thurnherr, A. M., Reverdin, G., Bouruet-Aubertot, P., and Roullet, G.: Deep Currents in the Rift Valley of the North Mid-Atlantic Ridge, Frontiers in Marine Science, 6, 17, https://doi.org/10.3389/fmars.2019.00597, 2019.

Lavelle, J. W., Cowen, J. P., and Massoth, G. J.: A model for the deposition of hydrothermal manganese near ridge crests, J. Geophys. Res.-Oceans, 97, 7413–7427, https://doi.org/10.1029/92JC00406, 1992.

Lough, A. J. M., Klar, J. K., Homoky, W. B., Comer-Warner, S. A., Milton, J. A., Connelly, D. P., James, R. H., and Mills, R. A.: Opposing authigenic controls on the isotopic signature of dissolved iron in hydrothermal plumes, Geochim. Cosmochim. Ac., 202, 1–20, https://doi.org/10.1016/j.gca.2016.12.022, 2017.

Lough, A. J. M., Homoky, W. B., Connelly, D. P., Comer-Warner, S. A., Nakamura, K., Abyaneh, M. K., Kaulich, B., and Mills, R. A.: Soluble iron conservation and colloidal iron dynamics in a hydrothermal plume, Chem. Geol., 511, 225–237, https://doi.org/10.1016/j.chemgeo.2019.01.001, 2019a.

Lough, A. J. M., Connelly, D. P., Homoky, W. B., Hawkes, J. A., Chavagnac, V., Castillo, A., Kazemian, M., Nakamura, K., Araki, T., Kaulich, B., and Mills, R. A.: Diffuse Hydrothermal Venting: A Hidden Source of Iron to the Oceans, Frontiers in Marine Science, 6, 14, https://doi.org/10.3389/fmars.2019.00329, 2019b.

Lupton, J. E. and Craig, H.: A Major Helium-3 Source at 15° S on the East Pacific Rise, Science, 214, 13–18, https://doi.org/10.1126/science.214.4516.13, 1981.

Lupton, J. E., Weiss, R. F., and Craig, H.: Mantle helium in hydrothermal plumes in the Galapagos Rift, Nature, 267, 603–604, https://doi.org/10.1038/267603a0, 1977.

Massoth, G. J., Baker, E. T., Lupton, J. E., Feely, R. A., Butterfield, D. A., Von Damm, K. L., Roe, K. K., and Lebon, G. T.: Temporal and spatial variability of hydrothermal manganese and iron at Cleft segment, Juan de Fuca Ridge, J. Geophys. Res.-Sol. Ea., 99, 4905–4923, https://doi.org/10.1029/93JB02799, 1994.

Millero, F. J., Sotolongo, S., and Izaguirre, M.: The Oxidation Kinetics of Fe(II) in Seawater, Geochim. Cosmochim. Ac., 51, 793–801, https://doi.org/10.1016/0016-7037(87)90093-7, 1987.

Milne, A., Schlosser, C., Wake, B. D., Achterberg, E. P., Chance, R., Baker, A. R., Forryan, A., and Lohan, M. C.: Particulate phases are key in controlling dissolved iron concentrations in the (sub)tropical North Atlantic, Geophys. Res. Lett., 44, 2377–2387, https://doi.org/10.1002/2016gl072314, 2017.

Mottl, M. J. and McConachy, T. F.: Chemical processes in buoyant hydrothermal plumes on the East Pacific Rise near 21° N, Geochim. Cosmochim. Ac., 54, 1911–1927, 1990.

Mottl, M. J.: Explanatory Notes and Master Chemical Item Spreadsheet for the VentDB Data Collections housed in the EarthChem Library, Version 1.0. Interdisciplinary Earth Data Alliance (IEDA), [data set], https://doi.org/10.1594/IEDA/100207 2012.

Nishioka, J., Obata, H., and Tsumune, D.: Evidence of an extensive spread of hydrothermal dissolved iron in the Indian Ocean, Earth Planet. Sc. Lett., 361, 26–33, https://doi.org/10.1016/j.epsl.2012.11.040, 2013.

Obata, H., Karatani, H., and Nakayama, E.: Automated determination of iron in seawater by chelating resin concentration and chemiluminescence detection, Anal. Chem., 65, 1524–1528, https://doi.org/10.1021/ac00059a007, 1993.

Pester, N. J., Reeves, E. P., Rough, M. E., Ding, K., Seewald, J. S., and Seyfried, W. E.: Subseafloor phase equilibria in high-temperature hydrothermal fluids of the Lucky Strike Seamount (Mid-Atlantic Ridge, 37° 17′ N), Geochim. Cosmochim. Ac., 90, 303–322, https://doi.org/10.1016/j.gca.2012.05.018, 2012.

Resing, J. A. and Mottl, M. J.: Determination of manganese in seawater using flow injection analysis with on-line preconcentration and spectrophotometric detection, Anal. Chem., 64, 2682–2687, https://doi.org/10.1021/ac00046a006, 1992.

Resing, J. A., Sedwick, P. N., German, C. R., Jenkins, W. J., Moffett, J. W., Sohst, B. M., and Tagliabue, A.: Basin-scale transport of hydrothermal dissolved metals across the South Pacific Ocean, Nature, 523, 200–203, https://doi.org/10.1038/nature14577, 2015.

Roshan, S., DeVries, T., Wu, J., John, S., and Weber, T.: Reversible scavenging traps hydrothermal iron in the deep ocean, Earth Planet. Sc. Lett., 542, 116297, https://doi.org/10.1016/j.epsl.2020.116297, 2020.

Saito, M. A., Noble, A. E., Tagliabue, A., Goepfert, T. J., Lamborg, C. H., and Jenkins, W. J.: Slow-spreading submarine ridges in the South Atlantic as a significant oceanic iron source, Nat. Geosci., 6, 775–779, https://doi.org/10.1038/ngeo1893, 2013.

Santana-Casiano, J. M., González-Dávila, M., Rodríguez, M. J., and Millero, F. J.: The effect of organic compounds in the oxidation kinetics of Fe(II), Mar. Chem., 70, 211–222, https://doi.org/10.1016/S0304-4203(00)00027-X, 2000.

Schine, C. M. S., Alderkamp, A.-C., van Dijken, G., Gerringa, L. J. A., Sergi, S., Laan, P., van Haren, H., van de Poll, W. H., and Arrigo, K. R.: Massive Southern Ocean phytoplankton bloom fed by iron of possible hydrothermal origin, Nat. Commun., 12, 1211, https://doi.org/10.1038/s41467-021-21339-5, 2021.

Schlitzer, R., Anderson, R. F., Dodas, E. M., Lohan, M., Geibert, W., Tagliabue, A., Bowie, A., Jeandel, C., Maldonado, M.

T., Landing, W. M., Cockwell, D., Abadie, C., Abouchami, W., Achterberg, E. P., Agather, A., Aguliar-Islas, A., van Aken, H. M., Andersen, M., Archer, C., Auro, M., de Baar, H. J., Baars, O., Baker, A. R., Bakker, K., Basak, C., Baskaran, M., Bates, N. R., Bauch, D., van Beek, P., Behrens, M. K., Black, E., Bluhm, K., Bopp, L., Bouman, H., Bowman, K., Bown, J., Boyd, P., Boye, M., Boyle, E. A., Branellec, P., Bridgestock, L., Brissebrat, G., Browning, T., Bruland, K. W., Brumsack, H.-J., Brzezinski, M., Buck, C. S., Buck, K. N., Buesseler, K., Bull, A., Butler, E., Cai, P., Mor, P. C., Cardinal, D., Carlson, C., Carrasco, G., Casacuberta, N., Casciotti, K. L., Castrillejo, M., Chamizo, E., Chance, R., Charette, M. A., Chaves, J. E., Cheng, H., Chever, F., Christl, M., Church, T. M., Closset, I., Colman, A., Conway, T. M., Cossa, D., Croot, P., Cullen, J. T., Cutter, G. A., Daniels, C., Dehairs, F., Deng, F., Dieu, H. T., Duggan, B., Dulaquais, G., Dumousseaud, C., Echegoyen-Sanz, Y., Edwards, R. L., Ellwood, M., Fahrbach, E., Fitzsimmons, J. N., Russell Flegal, A., Fleisher, M. Q., van de Flierdt, T., Frank, M., Friedrich, J., Fripiat, F., Fröllje, H., Galer, S. J. G., Gamo, T., Ganeshram, R. S., Garcia-Orellana, J., Garcia-Solsona, E., Gault-Ringold, M., George, E., Gerringa, L. J. A., Gilbert, M., Godoy, J. M., Goldstein, S. L., Gonzalez, S. R., Grissom, K., Hammerschmidt, C., Hartman, A., Hassler, C. S., Hathorne, E. C., Hatta, M., Hawco, N., Hayes, C. T., Heimbürger, L.-E., Helgoe, J., Heller, M., Henderson, G. M., Henderson, P. B., van Heuven, S., Ho, P., Horner, T. J., Hsieh, Y.-T., Huang, K.-F., Humphreys, M. P., Isshiki, K., Jacquot, J. E., Janssen, D. J., Jenkins, W. J., John, S., Jones, E. M., Jones, J. L., Kadko, D. C., Kayser, R., Kenna, T. C., Khondoker, R., Kim, T., Kipp, L., Klar, J. K., Klunder, M., Kretschmer, S., Kumamoto, Y., Laan, P., Labatut, M., Lacan, F., Lam, P. J., Lambelet, M., Lamborg, C. H., Le Moigne, F. A. C., Le Roy, E., Lechtenfeld, O. J., Lee, J.-M., Lherminier, P., Little, S., López-Lora, M., Lu, Y., Masque, P., Mawji, E., McClain, C. R., Measures, C., Mehic, S., Barraqueta, J.-L. M., van der Merwe, P., Middag, R., Mieruch, S., Milne, A., Minami, T., Moffett, J. W., Moncoiffe, G., Moore, W. S., Morris, P. J., Morton, P. L., Nakaguchi, Y., Nakayama, N., Niedermiller, J., Nishioka, J., Nishiuchi, A., Noble, A., Obata, H., Ober, S., Ohnemus, D. C., van Ooijen, J., O'Sullivan, J., Owens, S., Pahnke, K., Paul, M., Pavia, F., Pena, L. D., Peters, B., Planchon, F., Planquette, H., Pradoux, C., Puigcorbé, V., Quay, P., Queroue, F., Radic, A., Rauschenberg, S., Rehkämper, M., Rember, R., Remenyi, T., Resing, J. A., Rickli, J., Rigaud, S., Rijkenberg, M. J. A., Rintoul, S., Robinson, L. F., Roca-Martí, M., Rodellas, V., Roeske, T., Rolison, J. M., Rosenberg, M., Roshan, S., Rutgers van der Loeff, M. M., Ryabenko, E., Saito, M. A., Salt, L. A., Sanial, V., Sarthou, G., Schallenberg, C., Schauer, U., Scher, H., Schlosser, C., Schnetger, B., Scott, P., Sedwick, P. N., Semiletov, I., Shelley, R., Sherrell, R. M., Shiller, A. M., Sigman, D. M., Singh, S. K., Slagter, H. A., Slater, E., Smethie, W. M., Snaith, H., Sohrin, Y., Sohst, B., Sonke, J. E., Speich, S., Steinfeldt, R., Stewart, G., Stichel, T., Stirling, C. H., Stutsman, J., Swarr, G. J., Swift, J. H., Thomas, A., Thorne, K., Till, C. P., Till, R., Townsend, A. T., Townsend, E., Tuerena, R., Twining, B. S., Vance, D., Velazquez, S., Venchiarutti, C., Villa-Alfageme, M., Vivancos, S. M., Voelker, A. H. L., Wake, B., Warner, M. J., Watson, R., van Weerlee, E., Alexandra Weigand, M., Weinstein, Y., Weiss, D., Wisotzki, A., Woodward, E. M. S., Wu, J., Wu, Y., Wuttig, K., Wyatt, N., Xiang, Y., Xie, R. C., Xue, Z., Yoshikawa, H., Zhang, J., Zhang, P., Zhao, Y., Zheng, L., Zheng, X.-Y., Zieringer, M., Zimmer, L. A., Ziveri, P., Zunino, P., and Zurbrick, C.: The GEOTRACES Intermediate Data Product 2017, [data set], Chem. Geol., 493, 210–223, https://doi.org/10.1016/j.chemgeo.2018.05.040, 2018.

Severmann, S., Johnson, C. M., Beard, B. L., German, C. R., Edmonds, H. N., Chiba, H., and Green, D. R. H.: The effect of plume processes on the Fe isotope composition of hydrothermally derived Fe in the deep ocean as inferred from the Rainbow vent site, Mid-Atlantic Ridge, 36°14′ N, Earth Planet. Sc. Lett., 225, 63–76, https://doi.org/10.1016/j.epsl.2004.06.001, 2004.

Tagliabue, A. and Resing, J.: Impact of hydrothermalism on the ocean iron cycle, Philos. T. R. Soc. A, 374, 20150291, https://doi.org/10.1098/rsta.2015.0291, 2016.

Tagliabue, A., Bopp, L., Dutay, J. C., Chever, F., Jean Baptiste, P., Bucciarelli, E., Lannuzel, D., Remenyo, T., Sarthou, G., Aumont, O., Gehlen, M., and Jeandel, C.: Hydrothermal contribution to the oceanic dissolved iron inventory, Nature, 3, 252–256, https://doi.org/10.1038/ngeo818, 2010.

Tagliabue, A., Bowie, A. R., Boyd, P. W., Buck, K. N., Johnson, K. S., and Saito, M. A.: The integral role of iron in ocean biogeochemistry, Nature, 543, 51–59, https://doi.org/10.1038/nature21058, 2017.

Toner, B. M., Fakra, S. C., Manganini, S. J., Santelli, C. M., Marcus, M. A., Moffett, J., Rouxel, O., German, C. R., and Edwards, K. J.: Preservation of iron(II) by carbon-rich matrices in a hydrothermal plume, Nat. Geosci., 2, 197–201, https://doi.org/10.1038/ngeo433, 2009.

Toner, B. M., German, C. R., Dick, G. J., and Breier, J. A.: Deciphering the Complex Chemistry of Deep-Ocean Particles Using Complementary Synchrotron X-ray Microscope and Microprobe Instruments, Accounts Chem. Res., 49, 128–137, 2016.

Trocine, R. P. and Trefry, J. H.: Distribution and chemistry of suspended particles from an active hydrothermal vent site on the Mid-Atlantic ridge at 26° N, Earth Planet. Sc. Lett., 88, 1–15, https://doi.org/10.1016/0012-821x(88)90041-6, 1988.

Ussher, S. J., Achterberg, E. P., Sarthou, G., Laan, P., de Baar, H. J. W., and Worsfold, P. J.: Distribution of size fractionated dissolved iron in the Canary Basin, Mar. Environ. Res., 70, 46–55, https://doi.org/10.1016/j.marenvres.2010.03.001, 2010.

Vic, C., Gula, J., Roullet, G., and Pradillon, F.: Dispersion of deep-sea hydrothermal vent effluents and larvae by submesoscale and tidal currents, Deep-Sea Res. Pt. I, 133, 1–51, 2018.

von der Heyden, B. P., Roychoudhury, A. N., Mtshali, T. N., Tyliszczak, T., and Myneni, S. C. B.: Chemically and Geographically Distinct Solid-Phase Iron Pools in the Southern Ocean, Science, 338, 1199–1201, https://doi.org/10.1126/science.1227504, 2012.

Weber, T.: Southern Ocean Upwelling and the Marine Iron Cycle, Geophys. Res. Lett., 47, e2020GL090737, https://doi.org/10.1029/2020GL090737, 2020.

Wu, J. F., Wells, M. L., and Rember, R.: Dissolved iron anomaly in the deep tropical-subtropical Pacific: Evidence for long-range transport of hydrothermal iron, Geochim. Cosmochim. Ac., 75, 460–468, https://doi.org/10.1016/j.gca.2010.10.024, 2011.

Yucel, M., Gartman, A., Chan, C. S., and Luther, G. W.: Hydrothermal vents as a kinetically stable source of iron-sulphide-bearing nanoparticles to the ocean, Nat. Geosci., 4, 367–371, https://doi.org/10.1038/ngeo1148, 2011.